

# Is Linear Feedback on Smoothed Dynamics Sufficient for Stabilizing Contact-Rich Plans?

Yuki Shirai<sup>1,2</sup>, Tong Zhao<sup>2</sup>, H.J. Terry Suh<sup>3</sup>, Huaijiang Zhu<sup>2,4</sup>,  
Xinpei Ni<sup>2,5</sup>, Jiuguang Wang<sup>2</sup>, Max Simchowitz<sup>3</sup>, and Tao Pang<sup>2</sup>

**Abstract**—Designing planners and controllers for contact-rich manipulation is extremely challenging as contact violates the smoothness conditions that many gradient-based controller synthesis tools assume. Contact smoothing approximates a non-smooth system with a smooth one, allowing one to use these synthesis tools more effectively. However, applying classical control synthesis methods to smoothed contact dynamics remains relatively under-explored. This paper analyzes the efficacy of linear controller synthesis using differential simulators based on contact smoothing. We introduce natural baselines for leveraging contact smoothing to compute (a) open-loop plans robust to uncertain conditions and/or dynamics, and (b) feedback gains to stabilize around open-loop plans. Using robotic bimanual whole-body manipulation as a testbed, we perform extensive empirical experiments on over 300 trajectories and analyze why LQR seems insufficient for stabilizing contact-rich plans. The summary and the experiments videos can be found [here](#).

## I. INTRODUCTION

Dexterous manipulation is full of contact-rich interactions, enabling various tasks through complex frictional interactions [1], [2]. Historically, the non-smooth nature of contact has precluded a range of planning and control methods that rely on gradients of the dynamics. Recent advances have utilized *contact smoothing* — where non-smooth dynamics are replaced by a continuously differentiable proxy — to great effect as surrogate dynamics models for *planning* through contact [3], [4], [5], [6]. One may hope, then, that smoothing enables the use gradient-based *control*.

This work suggests that the above hope may face significant obstacles. We (1) introduce LQR control for contact manipulation via contact smoothing. Furthermore, we (2) present and analyze robust trajectory optimization, hoping that the generated trajectories are robust to the model errors accumulated by using a surrogate dynamics model for control, and thus more amenable to LQR. Then, we (3) extensively evaluate the performance of these methods, both in simulation and in hardware, on a bimanual whole-body manipulation as shown in Fig. 1. In short, we find:

*Despite its efficacy in planning through contact, dynamical smoothing alone is unsatisfactory as a means to obtaining linear control policies.*

Finally, we (4) identify the key factors leading to the inadequacies of linear control; namely, the *unilaterality* of contact, and the tendency of controllers to “push and pull” unless the dynamics are only very-slightly smoothed.

<sup>1</sup>University of California, Los Angeles, <sup>2</sup>RAI Institute (formerly Boston Dynamics AI Institute), <sup>3</sup>MIT CSAIL, <sup>4</sup>New York University, <sup>5</sup>Georgia Tech. This work was done during YS, HZ and XN’s internship at the RAI Institute. Correspondence to [yukishirai4869@g.ucla.edu](mailto:yukishirai4869@g.ucla.edu).

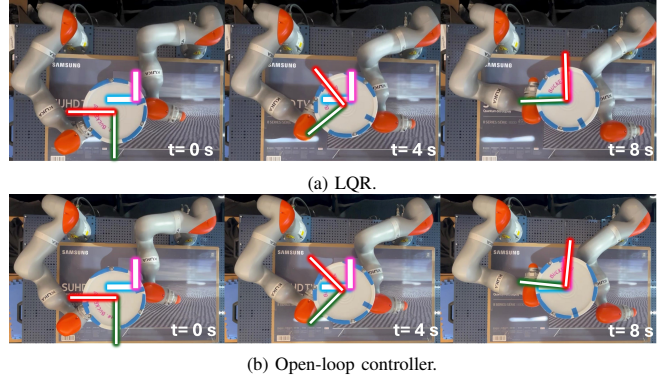


Fig. 1: These figures show snapshots of hardware experiments using LQR and open-loop controllers under perturbations to initial conditions of cylinder. The thick and thin lines represent the desired frame at the terminal time step and the current frame of the cylinder, respectively. While LQR outperforms open-loop in this example, a more comprehensive evaluation shows that LQR generally performs poorly. The hardware experiment videos can be found [here](#).

## II. RELATED WORK

### A. Planning through Contact

One approach to motion-planning through contact enforces contact dynamics by including linear complementarity constraints [7], [3], [8], [4], [9], [10]. Another popular method to address contacts is based on Mixed-Integer Programming (MIP) [11], [12], [13], [14], [15], where discrete variables encode contact modes. However, due to the inherent non-smoothness of contact dynamics, both methods suffer from poor scalability as the number of contact modes increases.

To tackle this, contact smoothing has been proposed, replacing exact dynamics models with surrogate models that obey second-order smoothness [3], [5], [16], [6]. This approach introduces a “force-at-a-distance” effect where gradients through the dynamics convey information about nearby contacts. Since gradients of the dynamics become continuous, gradient-based optimizers are able to find solutions more efficiently. Our work employs a log-barrier smoothing scheme [5], [6], which is more efficient compared to stochastic smoothing schemes [16], [17].

### B. Control through Contact

Prior approaches to control through contact reason about contact modes [18], [19], [20], [21]. While these approaches can run in real time for simple systems with only a handful of contact modes, they have yet to scale to high-dimensional systems, multiple objects per scene, or contacts with objects

of complex and/or irregular shapes due to the expensive computation.

In contrast, contact-smoothing offers a way to directly apply *smooth* control methods while being less constrained by the non-smoothness of contact dynamics, at the cost of introducing some smoothing bias [16]. In this work, we study LQR, which uses the underlying problem structure provided by contact smoothing, enabling its application to high-dimensional bimanual whole-body manipulation tasks.

### C. Robust Planning through Contact

Previous work on robust planning through contact (e.g., [22]) generally falls into two approaches: *domain randomization*, which involves stochastic optimization over a fixed distribution of dynamics models [21], [23], and *worst-case optimization*, which focuses on performance under worst-case scenarios within an uncertainty set [24], [25], [26], [27]. These methods effectively handle parametric uncertainties in the system dynamics, such as mass and friction, but do not discuss shape uncertainty (e.g., the radius of a cylinder). Shape uncertainty is critical for generalized manipulation to avoid unexpected contact events, yet integrating it into system dynamics remains challenging.

In this work, we incorporate domain randomization with an emphasis on shape uncertainty for primitive objects. Using contact smoothing, our method incorporates smoothed collision dynamics, enabling robust optimization to consider shape uncertainty. We also hope that using our technique enables LQR to track reference trajectories more easily.

## III. PROBLEM STATEMENT

We focus on the manipulation of rigid objects. Throughout, we focus on bimanual tabletop manipulation, though in principle our approach extends beyond this regime.

### A. Quasi-Dynamic Dynamics Model

We generate plans and linear feedback gains by considering a quasi-dynamic model of a robot manipulating a single rigid object [28]. We consider robots with  $n_a$  actuated Degrees of Freedom (DoFs) and the objects with  $n_u$  unactuated DoFs. We denote the configurations of the object and the robot as  $\mathbf{q}^u \in \mathbb{R}^{n_u}$  and  $\mathbf{q}^a \in \mathbb{R}^{n_a}$ , respectively. In quasi-dynamics models, we assume velocities are small, and thus system states are the concatenation of both configurations  $\mathbf{x} := \mathbf{q} := [\mathbf{q}^{u\top}, \mathbf{q}^{a\top}]^\top \in \mathbb{R}^{n_x}$ , where  $n_x = n_u + n_a$ .<sup>1</sup> We denote the change in system configuration from the current time step to the next time step as  $\delta\mathbf{q} := [\delta\mathbf{q}^{u\top}, \delta\mathbf{q}^{a\top}]^\top$ . We denote the control input as  $\mathbf{u} \in \mathbb{R}^{n_a}$ , defined as the commanded positions of the robot's joints. We consider the linear feedback law  $\mathbf{u} = \mathbf{v} + \mathbf{K}\Delta\mathbf{x}$  where  $\mathbf{v} \in \mathbb{R}^{n_a}$  is the feedforward gain from trajectory optimization,  $\mathbf{K} \in \mathbb{R}^{n_a \times n_x}$  is the feedback gain computed by LQR, and  $\Delta\mathbf{x}$  is the state error, or deviation from nominal trajectory.

<sup>1</sup>Superscript  $u$  stands for unactuated, and  $a$  for actuated.

### B. Quasi-Dynamic Dynamics Model with Contact Smoothing

For computing  $\delta\mathbf{q}$ , we consider a log-barrier-smoothed formulation of quasi-dynamic dynamics from Eq. (34) in [6]. We denote  $\kappa$ -smoothed forward dynamic map as

$$\mathbf{q}_{t+1} = f_\kappa(\mathbf{q}_t, \mathbf{u}_t) \quad (1)$$

where  $\kappa > 0$  is the user-defined barrier parameter. Smaller  $\kappa$  corresponds to greater contact smoothing, and more “force at a distance” [6]. Recalling our notation  $\mathbf{x} = \mathbf{q}$ , the above can also be written as  $\mathbf{x}_{t+1} = f_\kappa(\mathbf{x}_t, \mathbf{u}_t)$ . When  $\kappa$  does not change, we will simply write  $f$  for  $f_\kappa$ .

Both our gradient descent-based trajectory optimizer and our synthesis of linear feedback rely on differentiation of the smoothed dynamics. Given (1), we define derivatives:

$$\mathbf{A}_\kappa = \frac{\partial f_\kappa}{\partial \mathbf{q}}, \quad \mathbf{B} = \frac{\partial f_\kappa}{\partial \mathbf{u}}. \quad (2)$$

See [6] for the complete derivation of (2). Again, we use the shorthand  $\mathbf{A} = \mathbf{A}_\kappa$  and  $\mathbf{B} = \mathbf{B}_\kappa$ .

### C. Parametrized Quasi-Dynamic Dynamics Model

As described in Sec II-C, we consider *uncertainty over the dynamics* induced by object uncertainty. These can be parameterized by a parameter  $\mathbf{p} \in U \subseteq \mathbb{R}^{n_p}$  which enters into  $f_\kappa$  in (1). To lighten notation, we also let the parameter  $\mathbf{p}$  encode an initial condition,  $\mathbf{x}_{\text{init}}(\mathbf{p})$ .

## IV. CONTACT-IMPLICIT TRAJECTORY OPTIMIZATION

In this section, we present both single-parameter and multi-parameter trajectory optimization baselines.

### A. Single-Parameter Trajectory Optimization (SP-TrajOPT)

We formulate our optimal planning problem as follows.

$$\min_{\{\mathbf{x}_t\}_{t=1}^T, \{\mathbf{v}_t\}_{t=0}^{T-1}} J(\{\mathbf{x}_t\}_{t=1}^T, \{\mathbf{v}_t\}_{t=0}^{T-1}; \mathbf{p}) \quad (3a)$$

$$\text{s.t. } \mathbf{x}_{t+1} = f(\mathbf{x}_t, \mathbf{v}_t; \mathbf{p}), \forall t \in \mathcal{T} \quad (3b)$$

$$g(\mathbf{x}_t, \mathbf{v}_t; \mathbf{p}) \leq \mathbf{0}, \forall t \in \mathcal{T} \quad (3c)$$

$$\mathbf{x}_t \in \mathcal{X}, \mathbf{v}_t \in \mathcal{V}, \forall t \in \mathcal{T} \quad (3d)$$

$$\mathbf{x}_0 = \mathbf{x}_{\text{init}}(\mathbf{p}), \quad (3e)$$

where  $\mathcal{T} := \{0, \dots, T-1\}$ ,  $J$  is the trajectory-wise cost function,  $f = f_\kappa$  is the contact dynamics of the system (see (1)).  $\mathbf{v}_t$  is the control input at time step  $t$ . (3c) is used to impose inequality constraints involving  $\mathbf{x}_t$  and  $\mathbf{v}_t$  such as joint torque constraints and non-collision constraints.  $\mathcal{X}$  and  $\mathcal{V}$  represent a convex polytope, consisting of a finite number of linear inequality constraints for bounding the decision variables. In (3e), the initial condition encoded by  $\mathbf{p}^i$  determines the initial state  $\mathbf{x}_0$  (see Section III-C).

### B. Multi-Parameter Trajectory Optimization (MP-TrajOPT)

An alternative to (3) is a robust formulation over multiple parameters. We focus on the simplest approach: optimizing average performance on  $N$  realizations  $(\mathbf{p}^i)_{1 \leq i \leq N}$ , which for simplicity are manually chosen, inspired by [29], [21], using Sample Average Approximation (SAA) [30]. For each

$\mathbf{p}^i$ , we optimize over a corresponding trajectories  $(\mathbf{x}^i)_{1 \leq i \leq N}$ .

$$\min_{\mathbf{x}, \{\mathbf{v}_t\}_{t=0}^{T-1}} \frac{1}{N} \sum_{i=1}^N J(\{\mathbf{x}_t^i\}_{t=1}^T, \{\mathbf{v}_t\}_{t=0}^{T-1}; \mathbf{p}^i) \quad (4a)$$

$$\text{s.t. } \mathbf{x}_{t+1}^i = f_{\kappa}(\mathbf{x}_t^i, \mathbf{v}_t; \mathbf{p}^i), \forall t \in \mathcal{T}, \forall i \in \mathcal{I} \quad (4b)$$

$$g(\mathbf{x}_t^i, \mathbf{v}_t; \mathbf{p}^i) \leq \mathbf{0}, \forall t \in \mathcal{T}, \forall i \in \mathcal{I} \quad (4c)$$

$$\mathbf{x}_t^i \in \mathcal{X}, \mathbf{v}_t \in \mathcal{V}, \forall t \in \mathcal{T}, \forall i \in \mathcal{I} \quad (4d)$$

$$\mathbf{x}_0^i = \mathbf{x}_{\text{init}}(\mathbf{p}^i), \forall i \in \mathcal{I} \quad (4e)$$

where  $\mathbf{X} := \{\mathbf{x}_t^i, \forall t \in \mathcal{T}, \forall i \in \mathcal{I}\}$ ,  $\mathcal{I} := \{0, \dots, N-1\}$ . We emphasize that we do not have superscript  $i$  on  $\mathbf{v}_t$  because our objective is to design a single plan that succeeds on average over the  $N$  parameters. Note that (4) with  $N=1$  specializes to (3). We call this SP-TrajOPT (Single-Parameter Trajectory Optimization) as it only considers a single parameter. For  $N > 1$ , we refer to the procedure as MP-TrajOPT (Multi-Parameter Trajectory Optimization).

## V. FEEDBACK SYNTHESIS VIA LQR

In this section, we present an approach to feedback gain synthesis by solving an LQR problem through linearizations of the contact smoothed dynamics.

Using (2), we can compute LQR feedback gains  $\mathbf{K}$ . The objective of using LQR is to design a controller that can locally stabilize the system. In this work, we consider the following optimal control problem given  $\mathbf{x}_t$  and  $\mathbf{v}_t, t \in \mathcal{T}$ .

$$\min_{\{\Delta \mathbf{v}_t\}_{t=0}^{T-1}} \sum_{t=1}^T \|\Delta \mathbf{x}_t\|_{\mathbf{Q}_t}^2 + \sum_{t=0}^{T-1} \|\Delta \mathbf{v}_t\|_{\mathbf{R}_t}^2 \quad (5a)$$

$$\text{s.t. } \Delta \mathbf{x}_{t+1} = \mathbf{A}_t \Delta \mathbf{x}_t + \mathbf{B}_t \Delta \mathbf{v}_t, t \in \mathcal{T} \quad (5b)$$

$$\Delta \mathbf{x}_0 = \hat{\mathbf{x}} - \mathbf{x}_0 \quad (5c)$$

where  $\mathbf{Q}_t = \mathbf{Q}_t^{\top}$  is positive semidefinite and  $\mathbf{R}_t = \mathbf{R}_t^{\top}$  is positive definite at  $t$ .  $\hat{\mathbf{x}}$  is the measurement of states at  $t=0$ .  $\mathbf{A}_t$  and  $\mathbf{B}_t$  are error dynamics, which are obtained by linearizing true nonlinear contact dynamics of the system  $f$  around  $\mathbf{x}_t$  and  $\mathbf{v}_t, t \in \mathcal{T}$  in accordance with Sec.III-B. It is worth noting again that  $\mathbf{A}_t$  and  $\mathbf{B}_t$  convey local contact information of the system dynamics. We use Riccati recursion [31] to compute  $\mathbf{K}$  for (5). All of the computation happens offline. Hence, there is no expensive computation online unlike other methods (e.g., model predictive control).

## VI. RESULTS

In this section, we demonstrate our proposed controller under various uncertainties such as perturbations of initial conditions and shape variations for a cylinder. Through this section, we answer the following questions.

- 1) How well do TrajOPT and LQR work?
- 2) To what extent does MP-TrajOPT improve the performance of LQR?
- 3) Under what circumstances do our proposed controllers succeed or fail?

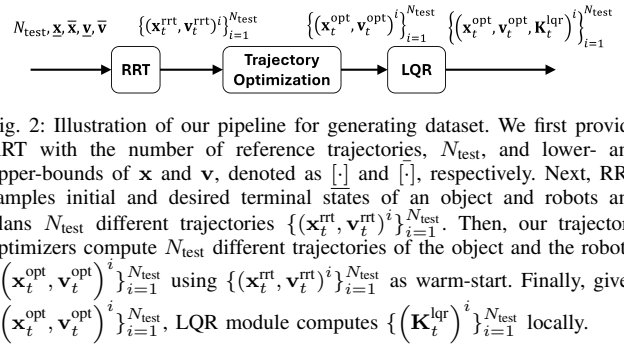


Fig. 2: Illustration of our pipeline for generating dataset. We first provide RRT with the number of reference trajectories,  $N_{\text{test}}$ , and lower- and upper-bounds of  $\mathbf{x}$  and  $\mathbf{v}$ , denoted as  $[\cdot]$  and  $\bar{[\cdot]}$ , respectively. Next, RRT samples initial and desired terminal states of an object and robots and plans  $N_{\text{test}}$  different trajectories  $\{(\mathbf{x}_t^{\text{rft}}, \mathbf{v}_t^{\text{rft}})\}_{i=1}^{N_{\text{test}}}$ . Then, our trajectory optimizers compute  $N_{\text{test}}$  different trajectories of the object and the robots,  $\{(\mathbf{x}_t^{\text{opt}}, \mathbf{v}_t^{\text{opt}})\}_{i=1}^{N_{\text{test}}}$  using  $\{(\mathbf{x}_t^{\text{rft}}, \mathbf{v}_t^{\text{rft}})\}_{i=1}^{N_{\text{test}}}$  as warm-start. Finally, given  $\{(\mathbf{x}_t^{\text{opt}}, \mathbf{v}_t^{\text{opt}})\}_{i=1}^{N_{\text{test}}}$ , LQR module computes  $\{(\mathbf{K}_t^{\text{lqr}})\}_{i=1}^{N_{\text{test}}}$  locally.

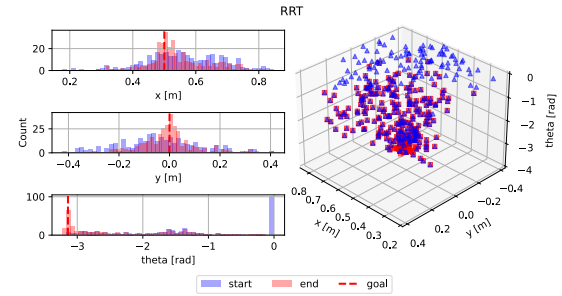


Fig. 3: Distribution of reference trajectories generated by RRT. **Left:** Histograms showing the distribution of the start and end configurations of the object in the RRT-generated trajectories. The goal object configuration of  $(0, 0, -\pi)$  is indicated. **Right:** 3D visualization of start and end object configurations of reference trajectories. While  $x$  and  $y$  coordinates are randomized,  $\theta$  is kept constant due to the cylinder's rotational symmetry.

### A. Experimental Setup

Three sets of parameters are in Table I. For SP-TrajOPT, we use the nominal “(a)” shape in that table; for MP-TrajOPT we use all  $N = 3$  “(a)”, “(b)” and “(c)” shapes. Our pipeline is depicted in Fig. 2. We begin by sampling  $N_{\text{test}} = 340$  reference trajectories using RRT in [6] with  $N_{\text{test}}$  different initial and goal states. RRT uses the nominal “(a)” parameter in Table I. These yield state and feedforward control input sequences,  $\{(\mathbf{x}_t^{\text{rft}}, \mathbf{v}_t^{\text{rft}})\}_{1 \leq t \leq T}^{N_{\text{test}}}$  as illustrated in Fig. 3. For each  $n = 1, \dots, N_{\text{test}}$ , we use  $\{(\mathbf{x}_t^{\text{rft}}, \mathbf{v}_t^{\text{rft}})\}_{1 \leq t \leq T}$  as a warm-start for computing trajectory-optimized plans  $\{(\mathbf{x}_t^{\text{opt}}, \mathbf{v}_t^{\text{opt}})\}_{1 \leq t \leq T}^{N_{\text{test}}}$ . The horizons  $T$  are determined by the RRT warm-start and vary across reference trajectories, but always lie in the range  $T \in [4, 64]$  with a mean of  $T = 26$ .

For SP-TrajOPT, we solve (3) under the nominal “(a)” parameter. For MP-TrajOPT, we solve (4) for all  $N = 3$  parameters (note that this produces  $N$  sequences of states; we select  $\mathbf{x}_t^{\text{opt}}$  to be the one under the nominal shape). Both use the following cost function:

$$\sum_{t=1}^T \|\mathbf{x}_t - \mathbf{x}_T^{\text{rft}}\|_{\mathbf{Q}_t}^2 + \sum_{t=0}^{T-1} \|\mathbf{v}_t\|_{\mathbf{R}_t}^2 \quad (6)$$

TABLE I: Parameters of cylinders.

	mass [kg]	friction coefficient	radius, length [m]
(a)	1.0	0.5	0.14, 0.5
(b)	1.0	0.5	0.13, 0.5
(c)	1.0	0.5	0.15, 0.5

where  $\mathbf{Q}_t = \text{diag}(10, 10, 10, 0.1, 0.1, 0.1, 0.1, 0.1, 0.1, 0.1)$ ,  $\mathbf{R}_t = \text{diag}(5, 5, 5, 5, 5, 5)$ ,  $\forall t \in [0, \dots, T-1]$ ,  $\mathbf{Q}_T = \text{diag}(1000, 1000, 1000, 0.1, 0.1, 0.1, 0.1, 0.1, 0.1, 0.1)$ . We formulate trajectory optimization programs using DRAKE’s MathematicalProgram [32] and solve them using SNOPT [33]. We optimize with dynamic smoothing parameter  $\kappa = 10^5$ . We use  $h = 0.1$  seconds as the time step.

### B. Feedback Synthesis

For LQR, we compute gains  $\{\mathbf{K}_t^{\text{lqr}}\}_{i=1}^{N_{\text{test}}}$  from  $\{(\mathbf{x}_t^{\text{opt}}, \mathbf{v}_t^{\text{opt}})\}_{i=1}^{N_{\text{test}}}$ . It means that, when the trajectories are supplied by SP- or MP-TrajOPT, gains are computed around the nominal parameter dynamics, (a) parameter in Table I. We use  $h = 0.1$  seconds as the time step, but use a smaller smoothing parameter,  $\kappa = 800$ , for smoother derivatives. We tune and set  $\mathbf{Q}_t = \text{diag}(10, 10, 10, 0.1, 0.1, 0.1, 0.1, 0.1, 0.1)$ ,  $\mathbf{R}_t = \text{diag}(5, 5, 5, 5, 5, 5)$ ,  $\forall t \in [0, \dots, T-1]$ ,  $\mathbf{Q}_T = \text{diag}(1000, 1000, 1000, 0.1, 0.1, 0.1, 0.1, 0.1, 0.1)$  to achieve good performance across  $N_{\text{test}}$  reference trajectories.

1) *Execution in DRAKE*: While plans and gains are synthesized via smoothed quasi-dynamic dynamics, we evaluate performance in either (i) DRAKE or (ii) on real hardware. The planning/feedback synthesis phase returns a sequence of states, feedforward control inputs, and feedback gains at discrete knot points  $(\{\mathbf{x}_t\}_{t=0}^T, \{\mathbf{v}_t\}_{t=0}^{T-1}, \{\mathbf{K}_t\}_{t=0}^{T-1})$ .

We adopt a higher control loop frequency in DRAKE simulations, which necessitates interpolation of these discrete-time quantities. To do so, we convert the knot points into continuous time using First-Order Hold (FOH): states  $\mathbf{x}^{\text{FOH}}(t)$ , feedforward control input  $\mathbf{v}^{\text{FOH}}(t)$ , and feedback control input trajectories  $\mathbf{K}^{\text{FOH}}(t)$ . For  $\mathbf{K}^{\text{FOH}}(t)$ , we interpolate elements of  $\mathbf{K}_t$  using FOH. At each time step in a DRAKE simulation, we measure the state  $\mathbf{x}^{\text{mea}}(t)$  and rollout out the controller  $\mathbf{u}(t) = \mathbf{v}^{\text{FOH}}(t) + \mathbf{K}^{\text{FOH}}(t) (\mathbf{x}^{\text{mea}}(t) - \mathbf{x}^{\text{FOH}}(t))$ .

2) *Evaluation Metrics*: To evaluate the performance of controllers, we define the following metrics:

$$\delta_{\text{terminal}} := d(\mathbf{x}_T^{\text{u,mea}}, \mathbf{x}_T^{\text{u,reference}}) \quad (7a)$$

$$\Delta_{\text{terminal}} := \frac{1}{N_{\text{test}}} \sum_{i=1}^{N_{\text{test}}} \delta_{\text{terminal}}^i \quad (7b)$$

$$\eta_A^B := \frac{\Delta_A^B}{\Delta_A^A} \quad (7c)$$

where  $\delta_{\text{terminal}}$  is the tracking error at the terminal time step. The superscript  $\text{u}$  extracts the elements corresponding to  $\mathbf{q}^{\text{u}}$  and  $\mathbf{x}_T^{\text{u,reference}}$  is the reference trajectory the controller tries to track. Through experiments, we consider  $\mathbf{x}_T^{\text{u,reference}} = \mathbf{x}_T^{\text{u,rrt}}$ .  $d(\cdot, \cdot)$  computes the Cartesian and angular displacements between two object poses. Given  $N_{\text{test}}$  reference trajectories computed from RRT,  $\delta_{\text{terminal}}^i$  shows that it is the tracking error of the  $i$ -th result.  $\Delta_{\text{terminal}}$  represents the average terminal tracking error over  $N_{\text{test}}$  demonstrations. Given two  $\Delta_{\text{terminal}}^A$  and  $\Delta_{\text{terminal}}^B$  obtained from controller A and B respectively, relative cost,  $\eta_A^B$  represents how much the tracking errors are different between controller A and B.

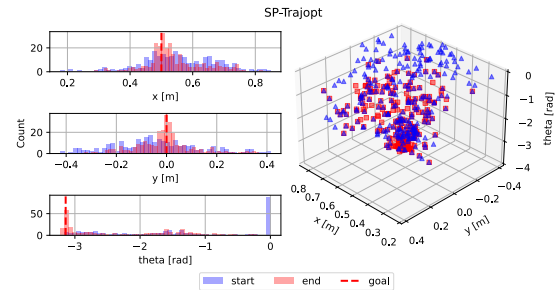


Fig. 4: Reference trajectories on which SP-TrajOPT ran successfully.

3) *Hardware Setup*: We use two 7-DoF Kuka iiwa arms for the hardware experiments. The robots run a joint impedance controller. We use a motion capture system to measure the state of the objects.

### C. Robustness Tests

To evaluate the robustness of controllers, we consider the perturbations to initial states and the radius of the cylinder.

1) *Robustness to Initial Condition*: After we obtain  $\mathbf{x}^{\text{FOH}}(t), \mathbf{v}^{\text{FOH}}(t), \mathbf{K}^{\text{FOH}}(t)$  (see Section VI-B.1), we add perturbations  $(\delta x, \delta y, \delta \theta)$  to the initial states of cylinder in DRAKE (i.e.,  $\mathbf{x}^{\text{u,mea}}(0) \leftarrow \mathbf{x}^{\text{u,mea}}(0) + [\delta x, \delta y, \delta \theta]^T$ ) and then we start rolling out the controller in DRAKE. We consider 50 points  $(\delta x, \delta y, \delta \theta) \sim \text{Uniform}([-x_0, +x_0] \times [-y_0, +y_0] \times [-\theta_0, +\theta_0])$  per reference trajectory where  $x_0 = y_0 = 0.025$  m,  $\theta_0 = 5^\circ$ .

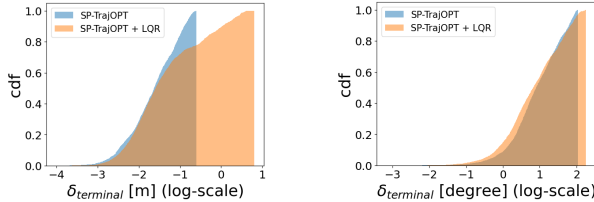
2) *Robustness to Variation in Shape*: After we obtain  $\mathbf{x}^{\text{FOH}}(t), \mathbf{v}^{\text{FOH}}(t), \mathbf{K}^{\text{FOH}}(t)$ , we add perturbations  $\delta r$  to the radius of cylinder,  $r$ , in DRAKE (i.e.,  $r \leftarrow r + \delta r$ ) and then we start rolling out the controller in DRAKE with this updated  $r$ . We consider 20 points  $\delta r \sim \text{Uniform}([-r_0, +r_0])$  per reference trajectory where  $r_0 = 0.01$  m.

### D. Results of SP-TrajOPT

Fig. 4 shows the coverage of SP-TrajOPT. Fig. 3 and Fig. 4 shows that SP-TrajOPT could successfully converge given reference trajectories by RRT. The success rate of SP-TrajOPT given 340 reference trajectories is 82.8%. We believe that this success rate is relatively high compared to other contact-implicit trajectory optimization frameworks. We think this is because the contact complementarity constraints are implicitly imposed through  $f_\kappa$  in our formulation. We also observe that the average position and orientation errors of the cylinder are reduced, from 0.18 m and  $71.9^\circ$  with RRT to 0.14 m and  $55.0^\circ$  with SP-TrajOPT, respectively. Hence, our SP-TrajOPT could successfully generate more optimal trajectories.

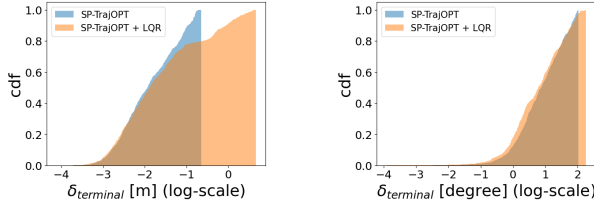
### E. Results of LQR with SP-TrajOPT

1) *Perturbations to Initial Conditions*: Fig. 5 shows SP-TrajOPT and LQR across variations of initial conditions for the cylinder. In Fig. 5a, SP-TrajOPT outperforms LQR. In Fig. 5b, both controllers show similar performance while SP-TrajOPT with LQR shows slightly better  $\Delta_{\text{terminal}}$ .



(a) Terminal position error,  $\Delta_{\text{terminal}}$  of SP-TrajOPT and SP-TrajOPT with LQR is 0.046 m and 0.30 m, respectively. (b) Terminal orientation error,  $\Delta_{\text{terminal}}$  of SP-TrajOPT and SP-TrajOPT with LQR is  $20.9^\circ$  and  $17.1^\circ$ .

Fig. 5: We evaluate terminal pose tracking error  $\delta_{\text{terminal}}$  of cylinder using SP-TrajOPT with / without LQR under perturbation of initial conditions. Note that cdf stands for cumulative distribution function.



(a) Terminal position error,  $\Delta_{\text{terminal}}$  of SP-TrajOPT and SP-TrajOPT with LQR is 0.034 m and 0.21 m, respectively. (b) Terminal orientation error,  $\Delta_{\text{terminal}}$  of SP-TrajOPT and SP-TrajOPT with LQR is  $19.7^\circ$  and  $20.2^\circ$ .

Fig. 6: We evaluate terminal pose tracking error  $\delta_{\text{terminal}}$  of cylinder using SP-TrajOPT with / without LQR under variation in shape.

**2) Perturbations to Shape:** The results of perturbations to the radius of the cylinder are shown in Fig. 6. SP-TrajOPT outperforms SP-TrajOPT with LQR in both position and orientation tracking errors.

### F. Results of MP-TrajOPT

Fig. 7 shows the coverage of MP-TrajOPT. Compared to the result of SP-TrajOPT in Fig. 4, we observe that MP-TrajOPT shows much smaller coverage. The success rate of MP-TrajOPT is 10.6 %, which is much lower than that of SP-TrajOPT. This is because MP-TrajOPT is much more complex than SP-TrajOPT, and thus, SNOPT might not be able to make any progress during optimization due to many reasons, such as poor scaling of the optimization problem.

### G. Results of LQR with MP-TrajOPT

**1) Perturbations to Initial Conditions:** The results of perturbations to initial conditions are shown in Fig. 8. While MP-TrajOPT outperforms MP-TrajOPT with LQR in Fig. 8a, the relative cost in Fig. 8a,  $\eta_{\text{MP-TrajOPT}}^{\text{MP-TrajOPT} + \text{LQR}} = 3.7$ . Since  $\eta$  in Fig. 5a is  $\eta_{\text{SP-TrajOPT}}^{\text{SP-TrajOPT} + \text{LQR}} = 6.5$ , we argue that MP-TrajOPT improves the LQR performance. For the orientation tracking error, Fig. 8b shows that MP-TrajOPT with LQR outperforms MP-TrajOPT while in Fig. 5b, SP-TrajOPT outperforms SP-TrajOPT with LQR. Therefore, we observe that MP-TrajOPT introduces some robustness, resulting in improved LQR performance. Also,  $\eta$  in Fig. 8b is  $\eta_{\text{MP-TrajOPT}}^{\text{MP-TrajOPT} + \text{LQR}} = 0.58$  while  $\eta$  in Fig. 5b is  $\eta_{\text{SP-TrajOPT}}^{\text{SP-TrajOPT} + \text{LQR}} = 0.82$ . Although our MP-TrajOPT is not designed to be robust against variation in initial conditions, the result suggests that the inherent robustness against parametric uncertainty of the model contributes to robustness under variation in initial conditions.

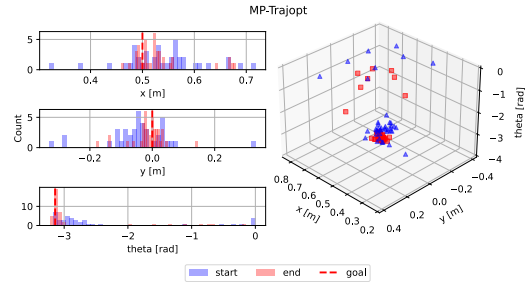
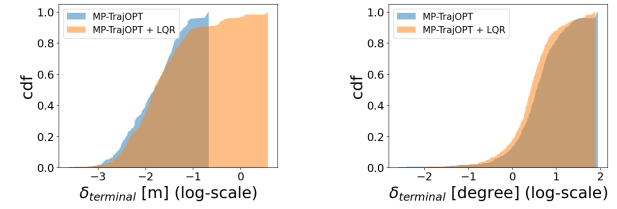


Fig. 7: Reference trajectories on which MP-TrajOPT ran successfully.



(a) Terminal position error,  $\Delta_{\text{terminal}}$  of MP-TrajOPT and MP-TrajOPT with LQR is 0.027 m and 0.10 m, respectively. (b) Terminal orientation error,  $\Delta_{\text{terminal}}$  of MP-TrajOPT and MP-TrajOPT with LQR is  $8.9^\circ$  and  $5.2^\circ$ .

Fig. 8: We evaluate terminal pose tracking error  $\delta_{\text{terminal}}$  of cylinder using MP-TrajOPT with / without LQR under perturbation of initial conditions.

**2) Perturbations to Shape:** The results are shown in Fig. 9. We observe that the performance of LQR improves. The relative cost in Fig. 9a and Fig. 6a is  $\eta_{\text{MP-TrajOPT}}^{\text{MP-TrajOPT} + \text{LQR}} = 3.1$  and  $\eta_{\text{SP-TrajOPT}}^{\text{SP-TrajOPT} + \text{LQR}} = 6.2$ , respectively. Similarly, the relative cost in Fig. 9b and Fig. 6b is  $\eta_{\text{MP-TrajOPT}}^{\text{MP-TrajOPT} + \text{LQR}} = 0.77$  and  $\eta_{\text{SP-TrajOPT}}^{\text{SP-TrajOPT} + \text{LQR}} = 1.01$ , respectively. Therefore, we observe that MP-TrajOPT and LQR work synergistically. However, these improvements can be observed only when MP-TrajOPT is solved, which is often difficult.

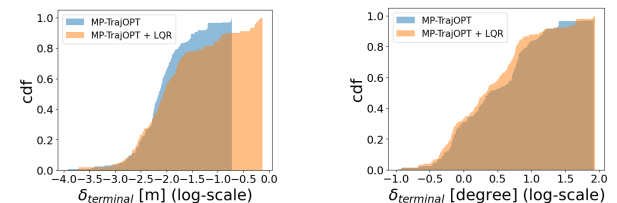
### H. Hardware Experiments

We implement two controllers, open-loop using SP-TrajOPT and LQR controllers, and evaluate their tracking performance in hardware experiments. As shown in Fig. 1, we observe that LQR could track the specific reference trajectory with perturbations to the initial states.

## VII. A CLOSER LOOK AT LQR

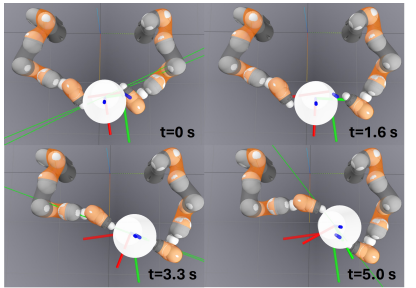
### A. Results of Different Smoothing

We discuss the relation between the behavior of LQR and the smoothing parameter  $\kappa$ . Here we have two results using LQR with  $\kappa = 160$  (i.e., more smoothing) and  $\kappa = 800$  (i.e.,

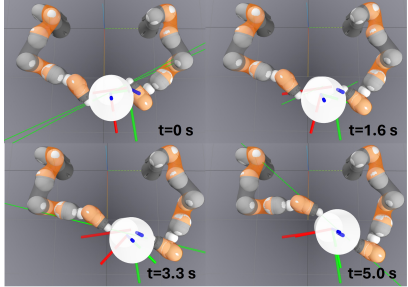


(a) Terminal position error,  $\Delta_{\text{terminal}}$  of MP-TrajOPT and MP-TrajOPT with LQR is 0.019 m and 0.059 m, respectively. (b) Terminal orientation error,  $\Delta_{\text{terminal}}$  of MP-TrajOPT and MP-TrajOPT with LQR is  $8.8^\circ$  and  $6.8^\circ$ .

Fig. 9: We evaluate terminal pose tracking error  $\delta_{\text{terminal}}$  of cylinder using MP-TrajOPT with / without LQR under variation in shape.



(a) Simulation result of LQR with cylinder with  $\kappa = 160$ .



(b) Simulation result of LQR with cylinder with  $\kappa = 800$ .

Fig. 10: Snapshots along a trajectory simulated in DRAKE. We implement LQR with the cylinder with different smoothing parameters  $\kappa$  for the same reference trajectory with the same initial condition perturbations. The snapshots show the cylinder frame and the desired frame at the terminal time step. Green lines represent contact forces. At  $t = 1.6$  s, the right arm in Fig. 10a loses the contact and causes *pulling* motion while the right arm in Fig. 10b maintains the contact. As a result, LQR in Fig. 10a fails to track the reference trajectory while LQR in Fig. 10b could successfully track it.

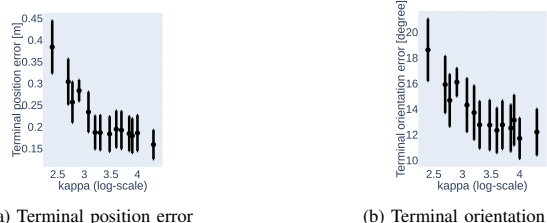


Fig. 11: Terminal pose tracking error  $\Delta_{\text{terminal}}$  with different smoothing values  $\kappa$  using LQR with perturbations of initial conditions. In the figures, we show the bar indicating the mean and 95% confidence interval.

less smoothing) for the same reference trajectory with the same perturbations of initial conditions used in Section VI-C.1. Fig. 10 shows the snapshots along the trajectory during the simulation in DRAKE.

With  $\kappa = 160$ , LQR makes the robot try to pull the cylinder even with no contact at  $t = 1.6$  s in Fig. 10a due to large contact smoothing. Through the experiments, we observe that a common rule of thumb for designing LQR with good tracking performance is to choose a large  $\kappa$  - if  $\kappa$  is too small, the controller will cause undesired pushing and *pulling* motion of the robot as shown in Fig. 11.

### B. Fundamental Shortcomings of Linearization

We here analyze why LQR does not work well on top of SP-TrajOPT-generated trajectories. One limitation of LQR is that the linearization does not sufficiently capture the *unilateral* nature of contact. To illustrate this, we consider a 1-step LQR problem in (8),

$$\min_{\Delta \mathbf{v}_0} \|\Delta \mathbf{x}_1\|_{\mathbf{P}_1}^2 \quad (8a)$$

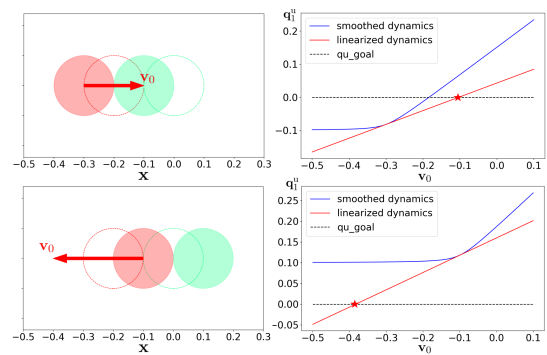


Fig. 12: Illustration of how LQR behaves in a 1D ball-pushing environment, where a red actuated ball tries to push a green unactuated ball using control inputs derived from LQR. The dotted balls in the left column denote the nominal state where linearization is done, and the solid balls illustrate the current state. The right columns illustrate the smoothed dynamics, linearized dynamics, and the optimal LQR solution according to linearization. The top row and bottom row illustrate two cases of disturbances, where the top row can be stabilized by pushing, but the bottom row requires pulling.

$$\text{s.t. } \Delta \mathbf{x}_1 = \mathbf{A}_0 \Delta \mathbf{x}_0 + \mathbf{B}_0 \Delta \mathbf{v}_0, \quad (8b)$$

$$\Delta \mathbf{x}_0 = \hat{\mathbf{x}} - \mathbf{x}_0. \quad (8c)$$

Consider a simple 1D block-pushing system (Fig. 12), where an actuated block is trying to push an unactuated block into a desired location. When we visualize the linearized dynamics in Fig. 12, we can observe that in cases where the red ball must *push* to stabilize, this 1-step LQR takes a step in the right direction although overshooting occurs (Fig. 12, top row). If we ask LQR to recover from overshooting (Fig. 12, bottom row), however, a linearized model predicts that it can pull the object and take a step towards the opposite direction. Yet, due to the directional nature of contact, this has no effect on the unactuated ball. This mismatch between the linearized model and the true model leads to limitations of the LQR controller. We observe this *pulling* motion in Fig. 10 in Section VII-A.

The symmetric nature of local linear models is fundamentally at odds with the unilateralness of contact. We address this challenge in [34], where we build a *trust region* in which the linearization is locally consistent with contact dynamics.

## VIII. CONCLUSION

Is linear feedback on smoothed dynamics sufficient for stabilizing contact-rich plans? Our analysis and experiments suggest that designing LQR for contact-rich plans does not work well in general. However, we observe that MP-TrajOPT enables LQR to improve its performance when MP-TrajOPT is solved, although MP-TrajOPT often fails to converge. Through this paper, we first present how contact smoothing technique can be used for designing trajectory optimization baselines and LQR. Then, we extensively conduct various experiments of LQR under different uncertainties. We hope that our analysis provides readers with insights into design of planners and controllers for contact-rich manipulation using differential simulators based on contact smoothing.

## ACKNOWLEDGEMENT

The authors would like to thank Hongkai Dai for insightful discussions on nonlinear optimization.

## REFERENCES

- [1] M. T. Mason, "Toward robotic manipulation," *Annual Review of Control, Robotics, and Autonomous Systems*, vol. 1, pp. 1–28, 2018.
- [2] Y. Shirai, A. Raghunathan, and D. Jha, "Hierarchical contact-rich trajectory optimization for multi-modal manipulation using tight convex relaxations," in *2025 IEEE International Conference on Robotics and Automation*, 2025.
- [3] M. Posa, C. Cantu, and R. Tedrake, "A direct method for trajectory optimization of rigid bodies through contact," *Int. J. Rob. Res.*, vol. 33, no. 1, pp. 69–81, 2014.
- [4] A. Ö. Önal, P. Long, and T. Padir, "Contact-implicit trajectory optimization based on a variable smooth contact model and successive convexification," in *2019 Int. Conf. Robot. Automat.*, 2019, pp. 2447–2453.
- [5] T. A. Howell, S. L. Cleac'h, J. Brüdigam, J. Z. Kolter, M. Schwager, and Z. Manchester, "Dojo: A differentiable physics engine for robotics," *arXiv preprint arXiv:2203.00806*, 2022.
- [6] T. Pang, H. T. Suh, L. Yang, and R. Tedrake, "Global planning for contact-rich manipulation via local smoothing of quasi-dynamic contact models," *IEEE Trans. Robot.*, vol. 39, no. 6, pp. 4691–4711, 2023.
- [7] D. E. Stewart and J. C. Trinkle, "An implicit time-stepping scheme for rigid body dynamics with inelastic collisions and coulomb friction," *International Journal for Numerical Methods in Engineering*, vol. 39, no. 15, pp. 2673–2691, 1996.
- [8] J. Carius, R. Ranftl, V. Koltun, and M. Hutter, "Trajectory optimization for legged robots with slipping motions," *IEEE Robot. Autom. Lett.*, vol. 4, no. 3, pp. 3013–3020, 2019.
- [9] A. Patel, S. L. Shield, S. Kazi, A. M. Johnson, and L. T. Biegler, "Contact-implicit trajectory optimization using orthogonal collocation," *IEEE Robot. Autom. Lett.*, vol. 4, no. 2, pp. 2242–2249, 2019.
- [10] S. H. Jeon, S. Kim, and D. Kim, "Online Optimal Landing Control of the MIT Mini Cheetah," in *2022 Int. Conf. Robot. Automat.*, 2022, pp. 178–184.
- [11] Y. Ding, C. Li, and H.-W. Park, "Kinodynamic motion planning for multi-legged robot jumping via mixed-integer convex program," in *2020 IEEE/RSJ Int. Conf. Intell. Rob. Syst.*, 2020, pp. 3998–4005.
- [12] A. Cauligi, P. Culbertson, B. Stellato, D. Bertsimas, M. Schwager, and M. Pavone, "Learning mixed-integer convex optimization strategies for robot planning and control," in *2020 59th IEEE Conference on Decision and Control (CDC)*, 2020, pp. 1698–1705.
- [13] T. Marcucci and R. Tedrake, "Warm start of mixed-integer programs for model predictive control of hybrid systems," *IEEE Transactions on Automatic Control*, vol. 66, no. 6, pp. 2433–2448, 2020.
- [14] Y. Shirai, X. Lin, A. Scherberg, Y. Tanaka, H. Kato, V. Vichathorn, and D. Hong, "Simultaneous contact-rich grasping and locomotion via distributed optimization enabling free-climbing for multi-limbed robots," in *2022 IEEE/RSJ Int. Conf. Intell. Rob. Syst.*, 2022, pp. 13 563–13 570.
- [15] P. M. Wensing, M. Posa, Y. Hu, A. Escande, N. Mansard, and A. D. Prete, "Optimization-Based Control for Dynamic Legged Robots," *IEEE Trans. Robot.*, vol. 40, pp. 43–63, 2024.
- [16] H. J. T. Suh, T. Pang, and R. Tedrake, "Bundled gradients through contact via randomized smoothing," *IEEE Robot. Autom. Lett.*, vol. 7, no. 2, pp. 4000–4007, 2022.
- [17] H. J. Suh, M. Simchowitz, K. Zhang, and R. Tedrake, "Do Differentiable Simulators Give Better Policy Gradients?" in *Proc. 2022 Int. Conf. Machine Learning*, vol. 162, 17–23 Jul 2022, pp. 20 668–20 696.
- [18] F. R. Hogan, E. R. Grau, and A. Rodriguez, "Reactive Planar Manipulation with Convex Hybrid MPC," in *2018 IEEE Int. Conf. Robot. Automat.*, 2018, pp. 247–253.
- [19] A. Aydinoglu and M. Posa, "Real-time multi-contact model predictive control via admm," in *2022 Int. Conf. Robot. Automat.*, 2022, pp. 3414–3421.
- [20] J. Moura, T. Stouraitis, and S. Vijayakumar, "Non-prehensile planar manipulation via trajectory optimization with complementarity constraints," in *2022 Int. Conf. Robot. Automat.*, 2022, pp. 970–976.
- [21] Y. Shirai, D. K. Jha, and A. U. Raghunathan, "Covariance Steering for Uncertain Contact-Rich Systems," in *2023 Int. Conf. Robot. Automat.*, 2023.
- [22] I. Mordatch, K. Lowrey, and E. Todorov, "Ensemble-cio: Full-body dynamic motion planning that transfers to physical humanoids," in *2015 IEEE/RSJ International Conference on Intelligent Robots and Systems (IROS)*. IEEE, 2015, pp. 5307–5314.
- [23] Y. Shirai, D. K. Jha, A. U. Raghunathan, and D. Romeres, "Chance-constrained optimization for contact-rich systems using mixed integer programming," *Nonlinear Analysis: Hybrid Systems*, vol. 52, p. 101466, 2024.
- [24] H. Dai and R. Tedrake, "Planning robust walking motion on uneven terrain via convex optimization," in *2016 IEEE-RAS Int. Conf. Humanoid Robots*, 2016, pp. 579–586.
- [25] R. Orsolino, M. Focchi, C. Mastalli, H. Dai, D. G. Caldwell, and C. Semini, "Application of wrench-based feasibility analysis to the online trajectory optimization of legged robots," *IEEE Robot. Autom. Lett.*, vol. 3, no. 4, pp. 3363–3370, 2018.
- [26] Y. Shirai, D. K. Jha, A. U. Raghunathan, and D. Romeres, "Robust pivoting: Exploiting frictional stability using bilevel optimization," in *2022 Int. Conf. Robot. Automat.*, 2022, pp. 992–998.
- [27] Y. Shirai, D. K. Jha, and A. U. Raghunathan, "Robust pivoting manipulation using contact implicit bilevel optimization," *IEEE Transactions on Robotics*, vol. 40, pp. 3425–3444, 2024.
- [28] M. Anitescu, "Optimization-based simulation of nonsmooth rigid multibody dynamics," *Mathematical Programming*, vol. 105, pp. 113–143, 2006.
- [29] L. Blackmore, M. Ono, A. Bektassov, and B. C. Williams, "A Probabilistic Particle-Control Approximation of Chance-Constrained Stochastic Predictive Control," *IEEE Trans. Robot.*, vol. 26, no. 3, pp. 502–517, 2010.
- [30] J. Luedtke and S. Ahmed, "A Sample Approximation Approach for Optimization with Probabilistic Constraints," *SIAM Journal on Optimization*, vol. 19, no. 2, pp. 674–699, 2008.
- [31] B. D. Anderson and J. B. Moore, *Optimal control: linear quadratic methods*. Courier Corporation, 2007.
- [32] R. Tedrake and the Drake Development Team, "Drake: Model-based design and verification for robotics," 2019. [Online]. Available: <https://drake.mit.edu>
- [33] P. E. Gill, W. Murray, and M. A. Saunders, "SNOPT: An SQP algorithm for large-scale constrained optimization," *SIAM review*, vol. 47, no. 1, pp. 99–131, 2005.
- [34] H. Suh, T. Pang, T. Zhao, and R. Tedrake, "Dexterous contact-rich manipulation via the contact trust region," *arXiv preprint arXiv:2505.02291*, 2025.